Light: Science & Applications (2017) 6, e17008; doi:10.1038/lsa.2017.8
Official journal of the CIOMP 2047-7538/17
www.nature.com/lsa

ORIGINAL ARTICLE

Real-time dynamics and cross-correlation gating spectroscopy of free-carrier Drude slow-light solitons

Heng Zhou[1,2,*], Shu-Wei Huang[2,3,*], Xiujian Li[2,4], James F McMillan[2], Chi Zhang[5], Kenneth Kin-Yip Wong[5], Mingbin Yu[6], Guo-Qiang Lo[6], Dim-Lee Kwong[6], Kun Qiu[1] and Chee Wei Wong[2,3]

Optical solitons—stable waves balancing delicately between nonlinearities and dispersive effects—have advanced the field of ultrafast optics and dynamics, with contributions spanning from supercontinuum generation to soliton fission, optical event horizons, Hawking radiation and optical rogue waves, among others. Here, we investigate picojoule soliton dynamics in silicon slow-light, photonic-bandgap waveguides under the influence of Drude-modeled, free-carrier-induced nonlinear effects. Using real-time and single-shot amplified dispersive Fourier transform spectroscopy simultaneously with high-fidelity cross-correlation frequency resolved optical gating at femtojoule sensitivity and femtosecond resolution, we examine the soliton stability limits, the soliton dynamics including free-carrier quartic slow-light scaling and acceleration, and the Drude electron–hole plasma-induced perturbations in the Cherenkov radiation and modulation instability. Our real-time single-shot and time-averaged cross-correlation measurements are matched with our detailed theoretical modeling, examining the reduced group velocity free-carrier kinetics on solitons at the picojoule scale.

Light: Science & Applications (2017) **6,** e17008; doi:10.1038/lsa.2017.8; published online 30 June 2017

Keywords: nonlinear kinetics; optical solitons; photonic bandgap materials

INTRODUCTION

Solitons are stable wave packets that emerge from the autonomous balance between dispersive and nonlinear phase shifts[1,2]. They have been examined in diverse media including various optical fibers[3–8], photonic crystal (PhC) waveguides[9–11], nonlinear photonic lattices[12] and resonant cavities[13,14]. The formation and propagation of solitons precisely reflect the physical characteristics of the operating regimes, with the key dynamics including the Raman-induced soliton self-frequency shift[3,4], soliton fission and compression[5,9,10], four-wave mixing[15], optical Cherenkov radiation[16–18], supercontinuum generation[4,6,16], optical rogue waves and fluctuations[19,20], astronomical-distance interactions of solitons[21], self-similarity[22] and event horizon analogs[8], among others[23]. At the same time, advances in silicon photonic platforms, especially with slow-light PhC structures, provide a broad parameter space for soliton dynamics with their tailorable dispersion and enhanced Kerr nonlinearity[9–11,24–28]. The intrinsic two-photon absorption (TPA) property of single-crystal silicon when pumped with high peak power near-infrared lasers drives the high density of free carriers and its corresponding Drude plasma dynamics. This has been shown to induce soliton acceleration[10,29,30], soliton compression[31] and soliton fission[32] in PhC waveguides.

Here, we advance the dynamic studies of slow-light solitons on-chip with the inherent Drude electron–hole plasma nonlinearities through simultaneous real-time single-shot amplified dispersive Fourier transform (ADFT) and cross-correlation frequency resolved optical gating (XFROG) spectroscopies. First, a quartic slow-light scaling (at 7% the vacuum speed of light) of the free-carrier kinetics is described based on the high-fidelity XFROG characterization of solitary pulses. We provide closed-form analytical solutions together with the numerical modeling and measurements to describe the self-induced temporal acceleration and self-frequency blue-shift. Second, we extend the description of the Drude electron–hole plasma perturbations to femtosecond pulse spectrum broadening and optical Cherenkov radiation. We describe the soliton-to-soliton stability limits of the free-carrier plasma-induced spectral broadening via single-shot ADFT characterization in real time. In the presence of free-carrier dynamics, the soliton spectrum histograms demonstrate near-Gaussian limited intensity distributions with markedly high stability. Third, we investigate the free-carrier-perturbed modulation instability (MI) that occurs in both normal and anomalous dispersions, which has a broader gain spectrum and is thresholdless compared to the conventional Kerr MI. Our studies are matched with the resonance condition of Cherenkov radiation and the modified MI gain spectrum, including numeric and analytical solutions.

[1]Key Lab of Optical Fiber Sensing and Communication Networks, University of Electronic Science and Technology of China, Chengdu 611731, China; [2]Optical Nanostructures Laboratory, Columbia University, New York, NY 10027, USA; [3]Mesoscopic Optics and Quantum Electronics Laboratory, University of California, Los Angeles, CA 90095, USA; [4]College of Science, National University of Defense Technology, Changsha, Hunan 410073, China; [5]Department of Electrical and Electronic Engineering, The University of Hong Kong, Hong Kong, China and [6]Institute of Microelectronics, Agency for Science, Technology and Research, Science Park II, Singapore 117685, Singapore
*These authors contributed equally to this work.
Correspondence: H Zhou, Email: zhouheng@uestc.edu.cn; S-W Huang, Email: swhuang@seas.ucla.edu; CW Wong, Email: cheewei.wong@ucla.edu
Received 3 January 2017; revised 8 February 2017; accepted 8 February 2017; accepted article preview online 10 February 2017

MATERIALS AND METHODS

Figure 1a shows the hexagonal-lattice PhC fabricated with optimized photolithography in a foundry. The device is 250 nm thick, and the bottom SiO_2 cladding is 3 μm. The photonic bandgap nanomembrane, from an initial silicon-on-insulator wafer, has a periodicity, *a*, of 431 nm and a hole radius of 125 nm (0.290*a*). A single row translational defect is introduced, creating a 1.5 mm W1 slow-light PhC waveguide. The slow-light silicon PhC waveguide is then air-bridged by removing the bottom SiO_2 with buffered hydrogen fluoride (HF) etch. The group index n_g and group velocity dispersion (GVD) of the sample are measured with an optically clocked coherent swept wavelength interferometry[25]. In the swept wavelength interferometry, a fiber Mach-Zehnder interferometer with a 40 m path length imbalance is utilized to provide the base clock for the equidistant optical frequency sampling. In addition, the transmission spectrum of the hydrogen cyanide gas cell is acquired simultaneously as an absolute wavelength calibration to remove the synchronization errors and ensure the proper alignment of successive data sets. The resulting GVD and third-order dispersion are then extracted from the delay spectrogram and are shown in Figure 1a.

The pump pulse we use to interrogate the slow-light soliton dynamics is a 39 MHz repetition rate picosecond laser with a 2.3 ps full-width half-maximum pulse width (nearly transform limited), and its center wavelength is adjustable between 1545 and 1565 nm. A high-fidelity second-harmonic-generation based XFROG system (Figure 1b) is constructed to simultaneously capture the output pulse intensity, phase, and spectrum[33,34]. Due to the presence of a pre-defined and strong reference pulse, the temporal direction degeneracy is avoided in the XFROG measurement and can be used to characterize the weak pulses with sub-fJ sensitivity. In our setup, half of the pump pulse is tapped out before entering the PhC waveguide and is utilized as the reference pulse in the XFROG system. The temporal structure of the pump pulse is independently characterized *a priori* using a standard second-harmonic-generation FROG measurement system. The split and residual pump pulses are coupled into the PhC structure. The pulse output carries information of the slow-light soliton dynamics and is treated as the test pulse of the XFROG system. As shown in Figure 1b, our measurements avoid any pulse amplification, pulse distortion and optoelectronic conversion to ensure high-fidelity soliton characterization. Figure 1c shows an example XFROG spectrogram of the output pulse and the retrieved temporal pulse shape. To ensure proper convergence, the phase retrieval routine is concluded after the FROG error drops below 5×10^{-3} for all cases reported here[34].

Furthermore, we set up a single-shot spectrum measurement system based on the ADFT to study the shot-to-shot fluctuations of the subpicosecond slow-light soliton spectra at a repetition rate of 39 MHz (Refs. 35,36). In the ADFT set-up, a long spool of dispersion-compensating fiber encompassing a normal dispersion of 1.33 ns nm^{-1} is used to provide the necessary time stretching, as shown in Figure 1d, followed by a pre-amplifier along with a fast near-infrared photodiode–oscilloscope subsystem. The ADFT has an equivalent spectral resolution of 190 pm, and its fidelity is confirmed by comparing the averaged measurements with the spectra obtained from the optical spectrum analyzer (OSA). Before recording the time series of up to 4000 spectra, an averaged time-stretched spectrum (100 times) is captured and used as the reference spectrum for the

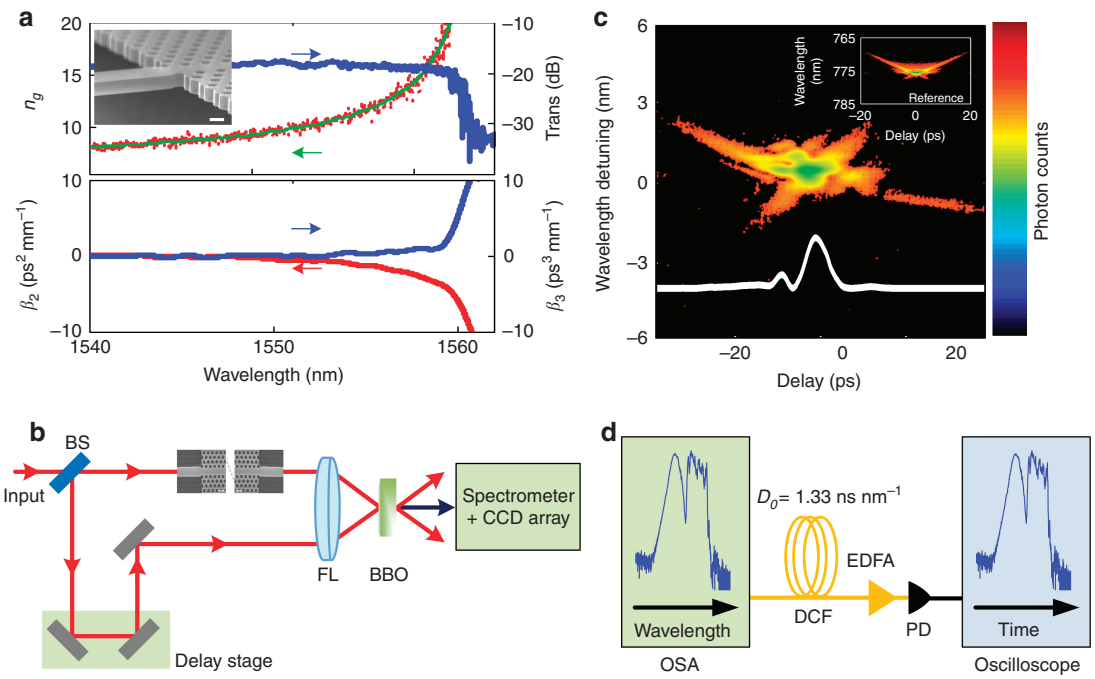

Figure 1 XFROG and real-time single-shot spectroscopy utilized to elucidate the Drude free-carrier soliton dynamics. (**a**) Group indices (data points with fitted green solid line), group velocity dispersion (red) and third-order dispersion (blue) of the slow-light PhC, measured via optically clocked swept wavelength interferometry. The waveguide transmission is shown in the upper panel (blue curve). The inset is the SEM image of the PhC, and the scale bar = 400 nm. (**b**) XFROG approach using second harmonics. (**c**) An illustrative XFROG spectrogram of the 1555 nm soliton at the output of the slow-light PhC waveguide. The retrieved intensity waveform is shown in white. The inset is the reference FROG spectrogram for the soliton measurements. (**d**) The ADFT set-up for real-time soliton characterization. BBO, barium borate nonlinear crystal; BS, beam splitter; DCF, dispersion compensation fiber; FL, focusing lens; PD, photodiode.

doi:10.1038/lsa.2017.8

cross-correlation analysis. The cross-correlation function is calculated using the definition:

$$C_{\mathrm{corr}}(\tau) = \frac{\int r(t)s(t-\tau)\mathrm{d}t}{\int |r(t)|^2\mathrm{d}t \int |s(t)|^2\mathrm{d}t} \quad (1)$$

where $r(t)$ denotes the reference spectrum and $s(t)$ denotes the single-shot spectrum.

To help gain physical insights into the slow-light soliton dynamics, we adopt the symmetric Fourier split step method to compute the non-integrable nonlinear Schrödinger equation (NLSE) with an auxiliary equation describing the free-carrier generation[26,31]:

$$\frac{\partial E}{\partial z} = -\alpha E + i\sum_{k\geq 2}\frac{\beta_k}{k!}\left(i\frac{\partial}{\partial t}\right)^k + i\left(s^2\gamma_{\mathrm{eff}}|E|^2 - sk_0k_cN_c\right)E \quad (2)$$

$$\alpha = \frac{\alpha_{\mathrm{linear}}}{2} + \frac{s^2\beta_{\mathrm{TPA}}}{2A_0}|E|^2 + sN_c\frac{\sigma}{2} \quad (3)$$

$$N_c = \int_{-\infty}^{T}\left(\frac{s^2\beta_{\mathrm{TPA}}}{2h\nu_0A_0^2}|E|^4 - \frac{N_c}{\tau_f}\right)\mathrm{d}t \quad (4)$$

Here, $s = n_{\mathrm{eff}}/n_o$ is the slow-light factor, β_k is the k-th order dispersion, α_{linear} is the PhC waveguide linear loss, $\gamma_{\mathrm{eff}} = 2\pi n_2/\lambda A_0$ is the Kerr nonlinear coefficient, β_{TPA} is the TPA coefficient, N_c is the TPA-generated free-carrier density, τ_f is the free-carrier lifetime, σ is the free-carrier absorption coefficient (FCA) and k_c is the free-carrier dispersion coefficient (FCD). The parameters used are illustrated in Table 1 and are from either our measurements (linear losses and dispersion of the PhC waveguide) or the published literature[26,31,37]. The precise input pulse shape is directly retrieved from the FROG measurement, providing the exact initial conditions for the NLSE modeling.

RESULTS AND DISCUSSION

Figure 1a plots the measured wavelength-dependent transmission and group index (upper panel), as well as the GVD and third-order dispersion of the PhC waveguide (lower panel). Within the PhC bandgap between 1540 and 1560 nm, the group index increases from 7.5 to 14.5 while the anomalous GVD can still support picosecond solitons. In this paper, we highlight the most heuristic soliton evolution results pumping at 1555 nm ($n_g = 10.0$, $\beta_2 = -1.6\ \mathrm{ps^2\,mm^{-1}}$, $\beta_3 = 0.22\ \mathrm{ps^3\,mm^{-1}}$) and 1560 nm ($n_g = 14.5$, $\beta_2 = -4.5\ \mathrm{ps^2\,mm^{-1}}$, $\beta_3 = 1.0\ \mathrm{ps^3\,mm^{-1}}$).

Figure 2 shows the retrieved pulse profiles and spectra as a function of the incident pulse energies. At 1555 nm, where the slow-light factor is relatively small, the output pulse exhibits flat phase profile and temporal compression to 2.1 ps. On the other hand, with increasing slow-light factor at 1560 nm, the soliton compression is absent but the output pulse exhibits a strikingly large temporal acceleration and self-frequency blue-shift. The temporal acceleration and the self-frequency blue-shift can be tuned continuously by changing the input pulse energy (Figure 3a). This leads to a maximum measured temporal acceleration as large as 6.4 ps, which is almost three times the input pulse width.

These measurements deterministically capture the pulse dynamics with combined temporal and spectral information and thus offer ideal platforms to understand the increased interactions in the large group index regime. Consequently, we model the pulse dynamics using the full-scale NLSE, which includes the slow-light scaling, exact device dispersion, TPA and dynamics of the free carriers. Slow-light enhancements in the Kerr nonlinearity and TPA, both of which are rooted in third-order nonlinearity, scale with s^2 (where s denotes the slow-light factor) because of the prolonged light–matter interaction time and increased light intensity because of spatial compression[27,37]. The slow-light enhancements of the FCD and FCA are, however, more subtle. First, the generated electrons and holes are from the TPA, and the carrier density scales quadratically with the laser intensity, which inherently scales with s^2 because of the intensity enhancement[37]. Second, the accumulation time (T in Equation (4)) and the polarizability (s in the last term of Equations (2) and (3)) of the free carriers are both affected by the prolonged interaction time, leading to another s^2 enhancement. This can give rise to an overall s^4 scaling of the FCA and FCD. These mechanisms can be viewed under the interpretation that the time-accumulated free-carrier generation, and the cascaded FCA and FCD provide more intense enhancements due to the slow-light compared with the Kerr nonlinearity, which is based on the instantaneous electric polarizability[38].

As shown in Figure 2a–2d, when s^4 scaling of the FCD and FCA is included in the model, remarkable agreements are achieved between theory and experiment for the soliton intensity, shape, phase, spectrum and acceleration. Note that the values of s for the wavelengths examined here ($s = 2.9$ for 1555 nm and $s = 4.2$ for 1560 nm) already reflect an ~70 to ~310 times scaling of the Drude free-carrier plasma effects, which are sufficient to manifest the underlying physics. To understand the slow-light scaling, we show the root-mean-square deviations between the experimentally measured and NLSE-calculated pulse intensity profiles and spectra under different scaling rules in Figure 2e and 2f. Unambiguously, with the s^4 enhancement for the free-carrier effects and the s^2 enhancement for both the Kerr and TPA, the smallest deviation of the temporal waveform and the spectra is obtained for a diverse array of soliton energies. This is especially true at the highest pulse energies that encounter the largest nonlinear contributions, supporting the quartic s^4 enhancement scaling of the Drude plasma nonlinearities in slow-light PhCs.

Furthermore, numerical modeling clearly shows that both the temporal acceleration and the self-frequency blue-shift originate from the slow-light-enhanced Drude free-carrier effect. Compared with the instantaneous Kerr effect, the nonlinear phase shift from the FCD results from the accumulation of free carriers generated from the TPA, resulting in a quasi-linear profile, as illustrated in Figure 3b. Consequently, the quasi-linear phase shift leads to a center frequency shift, and the temporal acceleration follows because of the anomalous dispersion. In addition, the cascaded nonlinear nature of the TPA–FCD process lends itself to more slow-light enhancements, leading to a more prominent effect at 1560 nm when the slow-light factor is

Table 1 Summary of parameters used in the NLSE simulations

Parameters	Values
Linear loss α_{linear}	2.5 dB mm^{-1}
Kerr nonlinear index n_2	5×10^{-18} m^2 W^{-1}
Effective nonlinear coefficient γ_{eff}	$\frac{2\pi n_2}{A_0\lambda}$
Two-photon absorption β_{TPA}	8.8×10^{-12} m W^{-1}
Free-carrier absorption σ	1.45×10^{-21} m^2
Free-carrier dispersion k_c	1.35×10^{-27} m^3
Modal area A_0	0.13 μm^2
Free-carrier lifetime τ_f	500 ps
Soliton number N	$\sqrt{\frac{s^2P_0\gamma_{\mathrm{eff}}T_0^2}{\lvert\beta_2\rvert}}$

Abbreviations: NSLE, nonlinear Schrödinger equation; TPA, two-photon absorption.

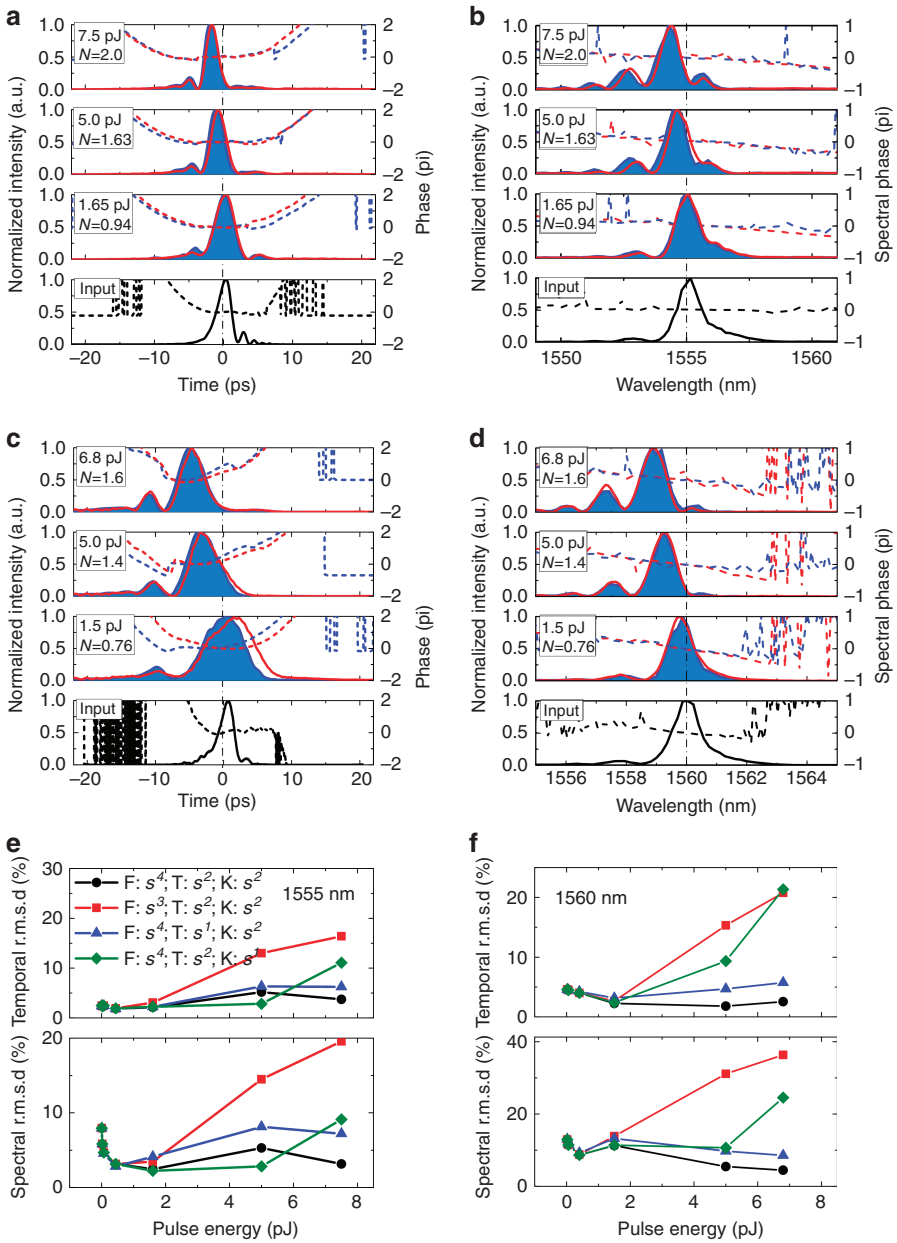

Figure 2 Quartic slow-light scaling of the Drude free-carrier nonlinear dynamics upon soliton propagation. The solitary dynamics are mapped with different input pulse energies and soliton numbers N for two example wavelengths of 1555 nm ($n_g = 10.0$) and 1560 nm ($n_g = 14.5$). (**a**,**b**) For 1555 nm, the blue-shaded area and blue dashed lines are the experimental cross-correlation-retrieved intensity and phase, respectively. The red dashed and solid line plots are the captured phase and intensity from the numerical predictions, respectively. (**c**,**d**) Same as (**a**,**b**) but for 1560 nm. In both center-wavelength cases, the soliton acceleration and self-frequency blue-shifts are observed at various magnitudes. (**e**,**f**) Measurement comparison with the pulse evolution modeling via NLSE including the Drude free-carrier dynamics elucidates the exponent in the slow-light scaling. Panel **e** is for the 1555 nm soliton and **f** is for the 1560 nm soliton. The top panel is the temporal measurement-theory RMSD. The bottom panel is the spectral measurement-theory RMSD. Letters in the legend are as follows: F, FCD and FCA dynamics; K, Kerr nonlinearities; RMSD, root-mean-square deviation; T, two-photon absorption.

higher. Moreover, Figure 3c illustrates that increasing the 1555 nm pulse energy to 25 pJ improves the pulse acceleration by up to 6 ps (more than 2.5× the pulse width) while maintaining a favorable pulse shape with modest compression. Further increases in the pulse energy split the soliton pulse.

To further understand the Drude soliton dynamics under slow-light enhancement, we next conduct the soliton perturbative analysis under the TPA–FCD. The detailed derivation of the perturbation is given in Supplementary Information Section I, and the results can be summarized in the following two closed-form equations for the self-frequency blue-shift and temporal acceleration:

$$\Delta\omega = \frac{4}{15}\frac{k_0 k_c \beta_{\mathrm{TPA}}}{h v_0 A_0^2} z \tag{5}$$

$$\Delta t = -\frac{2}{15}\frac{k_0 k_c \beta_{\mathrm{TPA}} |\beta_2|}{h v_0 A_0^2} z^2 \tag{6}$$

doi:10.1038/lsa.2017.8

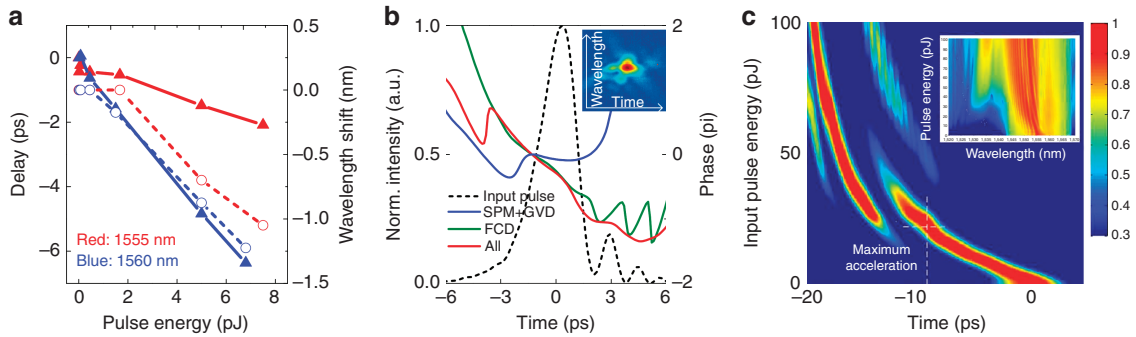

Figure 3 Influence of the Drude free-carrier dynamics on the slow-light soliton dynamics. (**a**) Under the Drude free-carrier perturbation, the measured soliton accelerations and self-frequency blue-shift are shown as the solid line with triangles and dashed lines with circles, respectively. The 1560 and 1555 nm slow-light examples are illustrated in blue and red. (**b**) The modeled contributing phase shifts are from the Drude free-carrier dynamics, self-phase modulation and group velocity dispersion. The input is a 1555 nm pulse at 7.5 pJ ($N=2.0$), with the pulse shape illustrated in the dashed background. The inset shows the corresponding measured XFROG spectrogram. (**c**) For a 1.5 mm slow-light photonic crystal waveguide, the maximum acceleration with an acceptable pulse shape is ~9.0 ps. The parameters used in the simulation are identical to those in Figure 2a and 2b. The insets show the corresponding spectral evolutions.

When the system parameters (Table 1) are entered, the estimated temporal acceleration from Equation (6) is 7.6 ps, which matches well with the experimentally measured acceleration of 6.4 ps for the 1560 nm pulse at 6.8 pJ. Of note, the effects of the FCD shown in Equation (5) are opposite to the self-frequency red-shift induced by Raman scattering in nonlinear optical fiber platforms[23]. While the Raman effect is more prominent when the system is interrogated by ultrashort laser pulses, the TPA–FCD effect is not changed with the input pulse duration if the fundamental soliton condition is satisfied. Hence, relatively long pulses, such as the 2.3 ps pulse used in this work, are preferred to observe the TPA–FCD effect in the absence of the Raman effect.

The Drude FCD also results in perturbations of the spectral broadening and optical Cherenkov radiation, as depicted in Figure 4. Figure 4a shows the experimentally measured spectral dynamics of the 780 fs (full-width at half-maximum) pulse. To facilitate the nonlinear spectral broadening of the femtosecond pulses, we utilize a PhC waveguide with a specifically designed low GVD regime near 1545 nm via symmetric lattice shift[39,40] (the GVD curve of this waveguide is differentiated slightly from the typical W1 PhC waveguide shown in Figure 1a, with the details given in Supplementary Information Section III). Here, the center wavelength is chosen at 1560 nm with $n_g \sim 14.0$ to harvest more slow-light enhancements in the FCD. As the input pulse energy is increased from 3.5 to 7.0 pJ, the 10-dB bandwidths are increased from 12.5 to 15.4, 22.2 and 25.1 nm. The measurements (blue solid lines) are well-matched to the NLSE numerical model (red solid lines). To identify the origin of the observed spectral broadening, we artificially turn off the FCD in the NLSE numerical model, and the magnitude of spectral broadening is greatly reduced (green dashed lines). While the Kerr nonlinearity is quenched by the nonlinear absorption in the silicon waveguide, the Drude TPA–FCD takes over and dominates the spectral broadening in our slow-light waveguide parameters.

To investigate the Drude free-carrier plasma-perturbed dynamics of Cherenkov radiation, Figure 4b shows the NLSE-simulated spectral broadening kinetics in our waveguide with a 7 pJ pulse energy and an approximate 780 fs pulse width. The FCD contribution is numerically tuned to evaluate its cumulative impact on the output spectra. Particularly, without the FCD, an isolated Cherenkov radiation side-band is obtained at ~1534.0 nm (≈50 dB smaller than the soliton spectrum), based on the zero-crossing of the dispersion near 1545 nm. When the FCD effect is numerically tuned to be larger, a clear blue-shift in the spectra is observed. Correspondingly, the dispersive wave manifests a red-shift to counterbalance this effect, cumulating in overlapped soliton and dispersive wave spectra. The mechanisms for such dynamics are multifold: first, a blue-shift of the soliton spectrum via the FCD corresponds to a red-shift of the phase-matched radiation spectrum[18]. Second, the blue-shifted soliton spectra overlap better with the red-shifted radiation components, leading to a rapid growth in the radiation intensity[16]. Third, the FCD modifies the phase-matching between the soliton and dispersive waves, enabling contributions to both the wavelength and intensity of the dispersive waves. In particular, the phase-matching condition of the Cherenkov radiation[6,18] is now modified by the FCD to:

$$\sum_{n\geq 2}\frac{\beta_n(\omega_S)(\omega_D-\omega_S)^n}{n!}=\phi_{SPM}+\phi_{FCD} \qquad (7)$$

where β_n is the nth order dispersion, ω_S and ω_D are the angular frequency of the soliton and dispersive wave emission, respectively, and ϕ_{SPM} and ϕ_{FCD} are the phase shift due to SPM and the FCD, respectively. Figure 4c shows the calculated phase-matching wavelengths with different values for the total nonlinear phase shift ($\phi_{SPM}+\phi_{FCD}$). First, with zero FCD and a soliton wavelength at 1560.0 nm (green spot 1 in Figure 4c), the analytically estimated phase-matching wavelength is ~1534.0 nm (yellow spot 1 in Figure 4c), which agrees well with the NLSE simulations (green and yellow spots 1 in Figure 4b, see Supplementary Information Section II). Increasing the FCD causes the Drude soliton spectrum to undergo a blue-shift (that is, ω_S becomes larger) while the phase shift from the FCD increases (that is, $\phi_{SPM}+\phi_{FCD}$ equals approximately $2s^2\gamma_{eff}P_o$ and $3s^2\gamma_{eff}P_o$ for spots 2 and 3, respectively), and the estimated resonance conditions are marked in Figure 4c (spots 2 and 3). These are also consistent with the numerical simulations shown in Figure 4b (spots 2 and 3, correspondingly) and our qualitative analysis above. Subsequently, with the FCD fully applied, the soliton spectrum and Cherenkov radiation emerge together. Therefore, in spite of the Cherenkov radiation not being distinctly separated from the soliton spectra, our analysis notes the underlying contribution and dynamics of the Cherenkov radiation perturbed by the Drude FCD. Furthermore, the FCD-induced Cherenkov radiation beneath the soliton spectrum is verified with the modeled time-domain waveform illustrated in

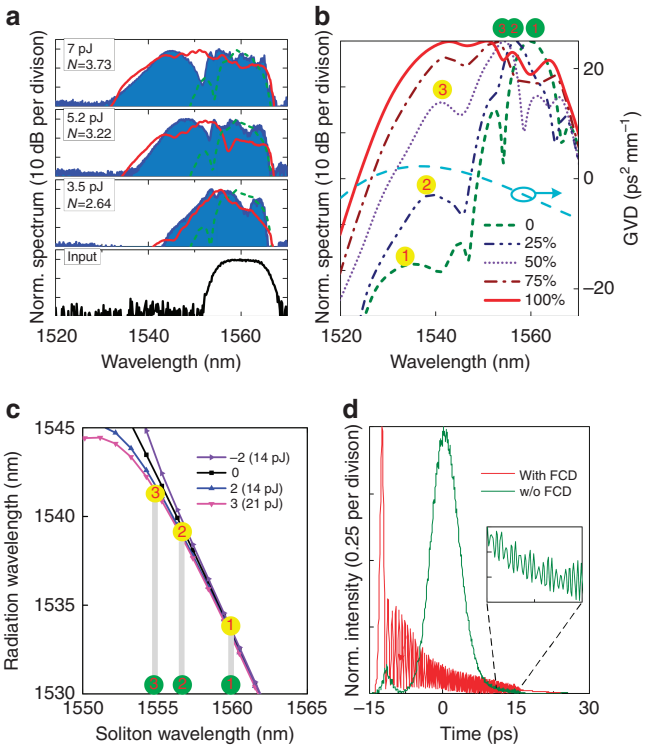

Figure 4 Drude FCD-based broadened spectra with optical Cherenkov radiation in the femtosecond soliton regime. (**a**) Experimental (blue) and NLSE simulated (red) spectral broadening with different pump pulse energies and solitary wave numbers *N*. Excellent agreement is achieved when the quartic slow-light scaling is included in the analysis. For illustrative comparison, dashed green lines show the NLSE simulated spectra when the FCD effect is numerically turned off. (**b**) The NLSE simulated spectra and dynamics from the Cherenkov radiation with increasing Drude FCD coefficient contributions. The estimated Cherenkov radiation peaks at the yellow spots 1–3 are 1534.0, 1538.5 and 1541.0 nm, and the corresponding soliton center wavelengths at the green spots 1–3 are 1560.0, 1556.7 and 1554.8 nm. The dispersion curve for the simulation is shown on the right vertical axis, with $\beta_2 = -3.5\ \mathrm{ps^2\ mm^{-1}}$, $\beta_3 = 0.5\ \mathrm{ps^3\ mm^{-1}}$, $\beta_4 = -0.005\ \mathrm{ps^4\ mm^{-1}}$ and $\beta_5 = -0.0025\ \mathrm{ps^5\ mm^{-1}}$, centered at 1560 nm. The zero crossing of the dispersion comes from the symmetrical lattice shift to build the low GVD region within the passband of the photonic crystal waveguide. (**c**) Analytically estimated phase-matching condition for Cherenkov radiation under different effective nonlinear phase shifts (corresponding pulse energy in the brackets), which are normalized to $s^2\gamma_{\mathrm{eff}}\ P_{\mathrm{o}}$. (**d**) The temporal waveform corresponding to the spectra shown in **b**, with the FCD both present and absent. The inset is the close-up signal of the temporal dispersive wave tails without the FCD, illustrating the faster and weaker temporal oscillations that arise from the heterodyne beating of the dispersive wave far separated from the soliton wave.

Figure 4d. Particularly, with the FCD applied, a larger but more slowly oscillating dispersive wave tail is obtained because of the overlapping of the Cherenkov and soliton spectra, in contrast to the smaller and more rapidly dispersive wave tail incurred by the far separated Cherenkov and soliton spectra without the Drude FCD.

With the spectral broadening induced by the slow-light-enhanced FCD, the ADFT is implemented to investigate the soliton-to-soliton stability of the broadened Drude soliton spectral components. Figure 5a shows the averaged optical spectra of the spectrally broadened pulses, measured with a grating-based OSA. The single-shot ADFT measurements are conducted on the pump not only at 1560 nm but also at 1540 nm, especially the spectral corners wherein any unstable features would be expected[41]. Figure 5b shows the recorded single-shot spectrum waveforms. The ADFT not only fully retrieves the detailed spectral characteristics but also unveils the real-time spectral dynamics that cannot be acquired in conventional OSAs or RF spectrum analyzers. Furthermore, Figure 5c summarizes the cross-correlation of the time-averaged (reference) spectra from the OSA and the single-shot spectra, where a near Gaussian spread around +1 containing minuscule instability is observed. The computed cross-correlation average values are $M_{\mathrm{fcd}} = 0.9989$ and $M_{\mathrm{pump}} = 0.9978$ for the FCD sideband and near the pump, respectively. Both values of variation ($V_{\mathrm{fcd}} = 3.4 \times 10^{-8}$ for the FCD sideband and $V_{\mathrm{pump}} = 2.0 \times 10^{-7}$ near the pump) are small and within the allowed instrumentation noise floor. This demonstrates the stable soliton-to-soliton behavior of the Drude TPA–FCD-induced spectral broadening, capturing the high stability of the Drude free-carrier nonlinear absorption (σ) and dispersion k_{c} parameters.

To further examine soliton dynamics under the Drude free-carrier plasma, we next theoretically and numerically examine the effects of the FCD on the MI gain spectrum. We assume:

$$E = \left[\sqrt{P} + a(z,t)\right] e^{i\left[\gamma_{\mathrm{eff}} P - \frac{k_0 k_{\mathrm{c}} \beta_{\mathrm{TPA}} \tau_{\mathrm{f}}}{2h\nu_0 A_0^2} P^2\right] z} \tag{8}$$

$$N_{\mathrm{c}} = \frac{\beta_{\mathrm{TPA}} \tau_{\mathrm{f}}}{2h\nu_0 A_0^2} P^2 + b(z,t) \tag{9}$$

where a and b are the perturbations. Here, the implicit assumption is that the absorption is not yet so strong that we can assume the steady-state solution has a constant amplitude along the propagation. This is a necessary approximation because no analytic steady-state solution exists if we consider all the dynamical absorptions. Using the linear stability analysis, we obtain the Drude-perturbed MI gain spectrum as (detailed in Supplementary Information Section IV):

$$G_{\mathrm{MI}} = \mathrm{Im}\left(|\beta_2 \Omega| \sqrt{\Omega^2 + \frac{4\gamma_{\mathrm{eff}} P}{\beta_2} - \frac{4 k_0 k_{\mathrm{c}} \beta_{\mathrm{TPA}} P^2}{h\nu_0 A_0^2 \beta_2 \left(\frac{1}{\tau_{\mathrm{f}}} - i\Omega\right)}}\right) \tag{10}$$

It is seen from Equation (10) that in contrast to the conventional Kerr MI utilized in optical parametric oscillators[23,42,43], the MI gain is always guaranteed by the Drude FCD regardless of the MI frequency and is present in both the normal and anomalous GVDs. Figure 6a shows the numerically calculated MI spectra with a 3 W continuous-wave pump. Agreeing with our analysis, the MI induced by the Drude FCD features a thresholdless amplification and a broader gain bandwidth. Furthermore, as shown in Figure 6b, in the normal dispersion region, the FCD-perturbed MI is possible, a result that is fundamentally different from that for the canonical Kerr MI, which only exists in the region of the anomalous GVD. In both regions, the spectra drop off with the increase in the frequency detuning due to the $1/\Omega$ term in Equation (10)[44]. Moreover, it is seen from Equation (10) that the MI perturbed by the FCD is affected by the free-carrier lifetime (the last term under the square root of Equation (10)), which is confirmed by the numerical simulations shown in Figure 6c. In particular, with a decreased τ_{f}, the numerically calculated MI spectra become narrower, which is consistent with the trend predicted by Equation (10). With zero free-carrier lifetime, the contribution from the FCD completely vanishes and the numerical MI spectrum turns into the pure Kerr case. Finally, Figure 6d shows the influence of the TPA on the MI gain spectrum. In particular, for the MI induced by the Kerr effect, the TPA loss severely suppresses the MI sidebands

doi:10.1038/lsa.2017.8

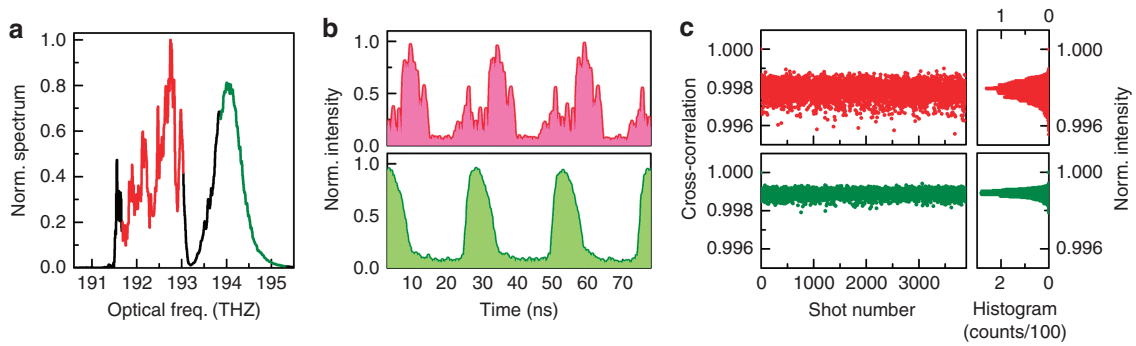

Figure 5 ADFT-based single-shot and real-time spectral measurements. (**a**) Averaged spectrum of the Drude FCD-induced spectral broadening and optical Cherenkov radiation, measured with an OSA. The soliton pulse energy is 7.0 pJ, and the center wavelength is at 1560 nm. (**b**) Example single-shot spectra corresponding to the red (near the pump wavelength) and green (the edge of the broadened spectrum) highlighted spectral components. The traces are captured using a real-time oscilloscope, with the temporal horizontal axis swapped to the optical spectra through the ADFT. (**c**) The single-shot spectra and time-averaged spectrum cross-correlation. Histograms of the cross-correlations demonstrate the nearly Gaussian spread around +1 with minuscule variations. The average cross-correlation for the Drude-broadened spectral sideband M_{fcd} is 0.9989, with a variation V_{fcd} of 3.4×10^{-8}. The cross-correlation mean value near the pump M_{pump} is 0.9978, with a variation V_{pump} of 2.0×10^{-7}. Both variation values are small and within the measurement noise floor, demonstrating stable soliton-to-soliton behavior.

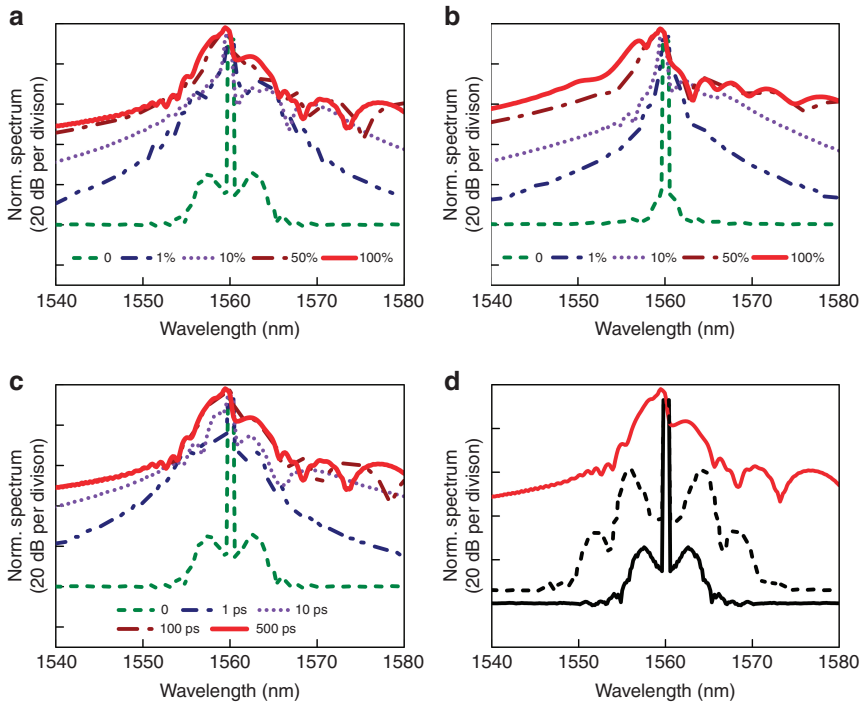

Figure 6 Theoretical study of the concurrent Drude FCD-perturbed MI in silicon photonic crystal waveguides. (**a**,**b**) NLSE simulated FCD perturbed MI spectra of a 3 W continuous wave pump for increasing FCD strength, (**a**) for the anomalous dispersion regime ($\beta_2=-2.2$ ps^2 mm^{-1}) and (**b**) for the normal dispersion regime ($\beta_2=2.2$ ps^2 mm^{-1}). (**c**) NLSE simulated FCD perturbed MI gain spectra for different free-carrier lifetimes in the anomalous dispersion regime ($\beta_2=-2.2$ ps^2 mm^{-1}). (**d**) Comparison of the influence of the TPA loss on the MI gain spectrum with (red) and without (black) the Drude FCD for a 3 W continuous wave pump in the anomalous dispersion regime ($\beta_2=-2.2$ ps^2 mm^{-1}). Solid lines show the cases with the TPA loss, and the dotted line shows the case without the TPA loss. Note that the solid red line does not have a corresponding dotted red line considering that the FCD must occur together with TPA. FCD, free-carrier dispersion.

because the Kerr MI originates from the parametric amplification that is directly proportional to the light intensity. However, if TPA is switched off for FCD-induced MI, the free-carrier densities drop to zero, collapsing the MI gain spectrum back to its original form. The uniqueness of the FCD-induced MI dynamics holds potential to realize on-chip broadband laser sources.

CONCLUSIONS

Here, we examined ultrafast solitary wave kinetics in slow-light silicon-based photonic bandgap waveguides based on ADFT real-time spectrum analysis and phase-resolved XFROG. With the slow-light-enhanced Kerr nonlinearity and Drude free-carrier effects, we demonstrated a quartic slow-light scaling of the Drude free-carrier

kinetics. Our high-fidelity measurements and analytical solutions captured the self-induced soliton acceleration, the self-frequency soliton blue-shift and the asymmetric spectral broadening under 780 fs pulse excitations. We further extended the Drude plasma perturbation model to broadband MI, illustrating a thresholdless MI gain spanning across the regions of normal and anomalous GVDs. The Drude dynamics also modified the resonance condition for Cherenkov radiation. To uncover the stability limits of the Drude dynamics, we subsequently examined the real-time and single-shot soliton-to-soliton dynamics through the ADFT. With the Drude plasma, the soliton histograms illustrate near-Gaussian limited distributions with pump and spectral sideband cross-correlations at the instrumentation noise limits. These observations advance fundamental insights into the combinational Drude plasma and Kerr dynamics of picojoule solitons in chip-scale silicon dispersive media.

CONFLICT OF INTEREST

The authors declare no conflict of interest.

ACKNOWLEDGEMENTS

We acknowledge discussions with and contributions by Pierre Colman, Bahram Jalali, Stefano Trillo, Jiangjun Zheng, Tingyi Gu, Jinghui Yang, Hao Zhou, Richard M Osgood Jr, Chad A Husko, Matthew D Marko, Pin-Chun Hsieh, Jiali Liao and Jiankun Yang. Funding support is from the Office of Naval Research with grant N00014-14-1-0041, and HZ acknowledges UESTC Young Faculty Award ZYGX2015KYQD051 and the 111 project (B14039). XL acknowledges funding from NSFC Grant 61070040. SWH acknowledges funding from AFOSR Young Investigator Award with grant FA9550-15-1-0081.

1 Christodoulides DN, Lederer F, Silberberg Y. Discretizing light behaviour in linear and nonlinear waveguide lattices. *Nature* 2003; **424**: 817–823.
2 Barland S, Tredicce JR, Brambilla M, Lugiato LA, Balle S *et al.* Cavity solitons as pixels in semiconductor microcavities. *Nature* 2002; **419**: 699–702.
3 Skryabin DV, Luan F, Knight JC, St J Russell P. Soliton self-frequency shift cancellation in photonic crystal fibers. *Science* 2003; **301**: 1705–1708.
4 Skryabin DV, Gorbach AV. *Colloquium*: looking at a soliton through the prism of optical supercontinuum. *Rev Mod Phys* 2010; **82**: 1287–1299.
5 Kibler B, Fatome J, Finot C, Millot G, Dias F *et al.* The Peregrine soliton in nonlinear fibre optics. *Nat Phys* 2010; **6**: 790–795.
6 Dudley JM, Genty G, Coen S. Supercontinuum generation in photonic crystal fiber. *Rev Mod Phys* 2006; **78**: 1135–1184.
7 Ouzounov DG, Ahmad FR, Müller D, Venkataraman N, Gallagher MT *et al.* Generation of megawatt optical solitons in hollow-core photonic band-gap fibers. *Science* 2003; **301**: 1702–1704.
8 Philbin TG, Kuklewicz C, Robertson S, Hill S, König F *et al.* Fiber-optical analog of the event horizon. *Science* 2008; **319**: 1367–1370.
9 Colman P, Husko C, Combrié S, Sagnes I, Wong CW *et al.* Temporal solitons and pulse compression in photonic crystal waveguides. *Nat Photonics* 2010; **4**: 862–868.
10 Husko CA, Combrié S, Colman P, Zheng JJ, De Rossi A *et al.* Soliton dynamics in the multiphoton plasma regime. *Sci Rep* 2013; **3**: 1100.
11 Blanco-Redondo A, de Sterke CM, Sipe JE, Krauss TF, Eggleton BJ *et al.* Pure-quartic solitons. *Nat Commun* 2016; **7**: 10427.
12 Fleischer JW, Segev M, Efremidis NK, Christodoulides DN. Observation of two-dimensional discrete solitons in optically induced nonlinear photonic lattices. *Nature* 2003; **422**: 147–150.
13 Herr T, Brasch V, Jost JD, Wang CY, Kondratiev NM *et al.* Temporal solitons in optical microresonators. *Nat Photon* 2014; **8**: 145–152.
14 Del'Haye P, Schliesser A, Arcizet O, Wilken T, Holzwarth R *et al.* Optical frequency comb generation from a monolithic microresonator. *Nature* 2007; **450**: 1214–1217.
15 Gorbach AV, Skryabin DV, Stone JM, Knight JC. Four-wave mixing of solitons with radiation and quasi-nondispersive wave packets at the short-wavelength edge of a supercontinuum. *Opt Express* 2006; **14**: 9854–9863.
16 Austin DR, de Sterke CM, Eggleton BJ, Brown TG. Dispersive wave blue-shift in supercontinuum generation. *Opt Express* 2006; **14**: 11997–12007.
17 Akhmediev N, Karlsson M. Cherenkov radiation emitted by solitons in optical fibers. *Phys Rev A* 1995; **51**: 2602–2607.
18 Colman P, Combrié S, Lehoucq G, de Rossi A, Trillo S. Blue self-frequency shift of slow solitons and radiation locking in a line-defect waveguide. *Phys Rev Lett* 2012; **109**: 093901.
19 Solli DR, Ropers C, Koonath P, Jalali B. Optical rogue waves. *Nature* 2007; **450**: 1054–1057.
20 Solli DR, Herink G, Jalali B, Ropers C. Fluctuations and correlations in modulation instability. *Nat Photon* 2012; **6**: 463–468.
21 Jang JK, Erkintalo M, Murdoch SG, Coen S. Ultraweak long-range interactions of solitons observed over astronomical distances. *Nat Photon* 2013; **7**: 657–663.
22 Dudley JM, Finot C, Richardson DJ, Millot G. Self-similarity in ultrafast nonlinear optics. *Nat Phys* 2007; **3**: 597–603.
23 Kivshar YS, Agrawal GP. *Optical Solitons: From Fibers to Photonic Crystals*. London: Academic Press. 2003.
24 Raineri F, Karle TJ, Roppo V, Monnier P, Raj P. Time-domain mapping of nonlinear pulse propagation in photonic-crystal slow-light waveguides. *Phys Rev A* 2013; **87**: 041802.
25 McMillan JF, Yu MB, Kwong DL, Wong CW. Observation of four-wave mixing in slow-light silicon photonic crystal waveguides. *Opt Express* 2010; **18**: 15484–15497.
26 Lin Q, Painter OJ, Agrawal GP. Nonlinear optical phenomena in silicon waveguides: modeling and applications. *Opt Express* 2007; **15**: 16604–16644.
27 Baba T. Slow light in photonic crystals. *Nat Photon* 2008; **2**: 465–473.
28 Corcoran B, Monat C, Grillet C, Moss DJ, Eggleton BJ *et al.* Green light emission in silicon through slow-light enhanced third-harmonic generation in photonic-crystal waveguides. *Nat Photon* 2009; **3**: 206–210.
29 Lefrancois S, Husko C, Blanco-Redondo A, Eggleton BJ. Nonlinear silicon photonics analyzed with the moment method. *J Opt Soc Am B* 2015; **32**: 218–226.
30 Blanco-Redondo A, Eades D, Li JT, Lefrancois S, Krauss TF *et al.* Controlling free-carrier temporal effects in silicon by dispersion engineering. *Optica* 2014; **1**: 299–306.
31 Blanco-Redondo A, Husko C, Eades D, Zhang Y, Li J *et al.* Observation of soliton compression in silicon photonic crystals. *Nat Commun* 2014; **5**: 3160.
32 Husko C, Wulf M, Lefrancois S, Combrié S, Lehoucq G *et al.* Free-carrier-induced soliton fission unveiled by *in situ* measurements in nanophotonic waveguides. *Nat Commun* 2016; **7**: 11332.
33 Power EP, March AM, Catoire F, Sistrunk E, Krushelnick K *et al.* XFROG phase measurement of threshold harmonics in a Keldysh-scaled system. *Nat Photon* 2010; **4**: 352–356.
34 Trebino R. *Frequency-Resolved Optical Gating: the Measurement of Ultrashort Laser Pulses*. New York: Kluwer. 2000.
35 Solli DR, Chou J, Jalali B. Amplified wavelength-time transformation for real-time spectroscopy. *Nat Photon* 2008; **2**: 48–51.
36 Goda K, Jalali B. Dispersive Fourier transformation for fast continuous single-shot measurements. *Nat Photon* 2013; **7**: 102–112.
37 Monat C, Corcoran B, Pudo D, Ebnali-Heidari M, Grillet C *et al.* Slow light enhanced nonlinear optics in silicon photonic crystal waveguides. *IEEE J Sel Top Quantum Electron* 2010; **16**: 344–356.
38 Baron A, Ryasnyanskiy A, Dubreuil N, Delaye P, Tran QV *et al.* Light localization induced enhancement of third order nonlinearities in a GaAs photonic crystal waveguide. *Opt Express* 2009; **17**: 552–557.
39 Hamachi Y, Kubo S, Baba T. Slow light with low dispersion and nonlinear enhancement in a lattice-shifted photonic crystal waveguide. *Opt Lett* 2009; **34**: 1072–1074.
40 Schulz SA, O'Faolain L, Beggs DM, White TP, Melloni A *et al.* Dispersion engineered slow light in photonic crystals: a comparison. *J Opt* 2010; **12**: 101004.
41 Wetzel B, Stefani A, Larger L, Lacourt PA, Merolla JM *et al.* Real-time full bandwidth measurement of spectral noise in supercontinuum generation. *Sci Rep* 2012; **2**: 882.
42 Tsoy EN, de Sterke CM, Abdullaev FK. Influence of two-photon absorption on modulational instability. *J Opt Soc Am B* 2001; **18**: 1144–1149.
43 Panoiu NC, Chen XG, Osgood RM. Modulation instability in silicon photonic nanowires. *Opt Lett* 2006; **31**: 3609–3611.
44 Zhou H, Liao ML, Huang SW, Zhou LJ, Qiu K *et al.* Six-wave mixing induced by free-carrier plasma in silicon nanowire waveguides. *Laser & Photonics Rev* 2016; **10**: 1054–1061.

This work is licensed under a Creative Commons Attribution-NonCommercial-NoDerivs 4.0 International License. The images or other third party material in this article are included in the article's Creative Commons license, unless indicated otherwise in the credit line; if the material is not included under the Creative Commons license, users will need to obtain permission from the license holder to reproduce the material. To view a copy of this license, visit http://creativecommons.org/licenses/by-nc-nd/4.0/

© The Author(s) 2017

Supplementary Information for this article can be found on the *Light: Science & Applications*' website (http://www.nature.com/lsa).